Sleep state-dependent modulations of hippocampal theta oscillations and sharp wave-ripples by pontine waves

Tomomi Tsunematsu[1,2,3], Sumire Matsumoto[2] and Shuzo Sakata[4]

[1] Super-network Brain Physiology, Graduate School of Life Sciences, Tohoku University, Sendai 980-8577, Japan

[2] Frontier Research Institute for Interdisciplinary Sciences, Tohoku University, Sendai 980-8578, Japan

[3] Precursory Research for Embryonic Science and Technology, Japan Science and Technology Agency, Kawaguchi 332-0012, Japan

[4] Strathclyde Institute of Pharmacy and Biomedical Sciences, University of Strathclyde, 161 Cathedral Street, Glasgow G4 0RE, UK

Correspondence (shuzo.sakata@strath.ac.uk)

Abstract

Ponto-geniculo-occipital (PGO) or pontine (P) waves are a prominent electrophysiological marker of rapid eye movement (REM) sleep. Although P-waves have long been recognized, they have been less studied compared to other sleep-related neural events. Recent studies in mice and macaques uncovered state-dependent functional coupling of P-waves with hippocampal oscillations, including sharp wave-ripples (SWRs) during non-REM (NREM) sleep and theta oscillations during REM sleep. However, the detailed characteristic of this functional coupling remains unclear. In addition, since P-waves in mice have been reported rarely, it is also important to describe their detailed electrophysiological properties, given the importance of the animal model. Here, we address these issues by performing multiple types of electrophysiological recordings in mice. P-waves characterized by diverse brainstem firing appear more frequently during REM sleep, and in both hemispheres at the same time across sleep states. The P-wave frequency can also predict the duration of REM sleep episodes. While P-waves induce modulated hippocampal excitability and phase coupling with theta oscillations during REM sleep, surprisingly P-waves lead to shorter SWRs during NREM sleep. These results suggest that P-waves play a role in systems memory consolidation by functionally coupling with hippocampal ensembles in a state-dependent fashion.

Keywords: REM sleep, NREM sleep, PGO wave, Sharp wave-ripples, Theta rhythms

Introduction

Sleep is a fundamental homeostatic process in the animal kingdom. Determining its characteristics and exploring its functions are fundamental in neuroscience. Sleep states in mammals can be determined by multiple electrophysiological markers. For example, in addition to low muscle tone, cortical electroencephalograms (EEGs) during NREM sleep are characterized by slow and delta (<4 Hz) oscillations. Additionally, other oscillations including sleep spindles and hippocampal sharp wave-ripples (SWRs) have been extensively studied (Adamantidis et al., 2019, Brown et al., 2012, Buzsaki, 2015, Byron et al., 2021, Steriade et al., 1993, Steriade, 2006).

While theta (~7 Hz) oscillations are prominent during REM sleep, ponto-geniculo-occipital (PGO) waves have long been recognized (Callaway et al., 1987, Datta, 1997, Jouvet et al., 1959, Brooks and Bizzi, 1963, Bizzi and Brooks, 1963b): PGO waves during REM sleep were initially reported in cats (Bizzi and Brooks, 1963a). Subsequently, similar sub-second brain waves have been observed in other mammalian species, including rats (Datta, 1997, Farber et al., 1980), mice (Patel et al., 2020, Tsunematsu et al., 2020), macaques (Ramirez-Villegas et al., 2021, Cohen and Feldman, 1968) and humans (Lim et al., 2007). In rats, PGO waves are often called as pontine-waves or “P-waves” (Datta, 2012).

P-waves consist of ~100 ms brain waves originated from mesopontine cholinergic nuclei, such as the pontine tegmental nucleus, laterodorsal tegmental nucleus and sublaterodorsal nucleus in rodents (Datta, 1997, Patel et al., 2020, Tsunematsu et al., 2020, Datta et al., 1998), which play an important role in REM sleep induction (Herice et al., 2019, Lu et al., 2006, Luppi et al., 2006, McCarley, 2007, Van Dort et al., 2015). P-waves can be observed across a wide range of brain regions, not just the visual pathway, but also in limbic areas (Calvo and Fernandez-Guardiola, 1984) and the cerebellum (Torres-Herraez et al., 2022, Jouvet et al., 1965).

During REM sleep, P-waves and hippocampal theta oscillations are coupled (Karashima et al., 2002, Ramirez-Villegas et al., 2021, Sakai et al., 1973, Tsunematsu et al., 2020): the timing of P-waves is locked to a certain phase of ongoing theta oscillations. While this was originally discovered in cats (Karashima et al., 2002, Sakai et al., 1973), recent studies confirmed in mice (Tsunematsu et al., 2020) and macaques (Ramirez-Villegas et al., 2021). P-waves can also be observed during NREM sleep although the frequency of P-waves is less (Ramirez-Villegas et al., 2021, Tsunematsu et al., 2020). Intriguingly, recent two studies in mice (Tsunematsu et al., 2020) and macaques (Ramirez-Villegas et al., 2021) reported that P-waves during NREM sleep are coupled with hippocampal SWRs, implying a role in systems memory consolidation. Although these results suggest brain-wide coordination of sleep-related neural events across sleep states, P-waves have been less studied, compared to other sleep-related neural events. In the present study, we performed several types of electrophysiological recordings in mice to determine the detailed characteristic of P-waves in mice and to examine how P-waves functionally interact with hippocampal activity across sleep states. We

report a non-trivial antagonistic role of P-waves with SWRs, suggesting the functional importance of P-waves in systems memory consolidation.

Results

P-waves in mice

We performed three types of electrophysiological recordings: firstly, we performed pontine EEG recording to detect P-waves by chronically implanting a bipolar electrode (*n* = 11 sessions from 6 animals) (**Fig. 1A**). Secondly, we performed silicon probe recording in mid-hindbrain regions (we call it as "brainstem" afterwards) to monitor spiking activity associated with P-waves (*n* = 9 sessions from 7 animals) (**Fig. 1D**). Finally, we performed silicon probe recording in the hippocampal CA1 while monitoring pontine EEGs to investigate the relationship between P-waves and hippocampal oscillations (*n* = 4 sessions from 2 animals) (**Fig. 5A**). Across all experiments, we also monitored cortical EEGs and electromyograms (EMGs) to determine sleep states. While we performed all experiments in a head-fixed condition since we combined silicon probe recording and pupillometry, the sleep architecture was generally comparable with that in a tethered unrestrained condition as reported previously (Tsunematsu et al., 2020).

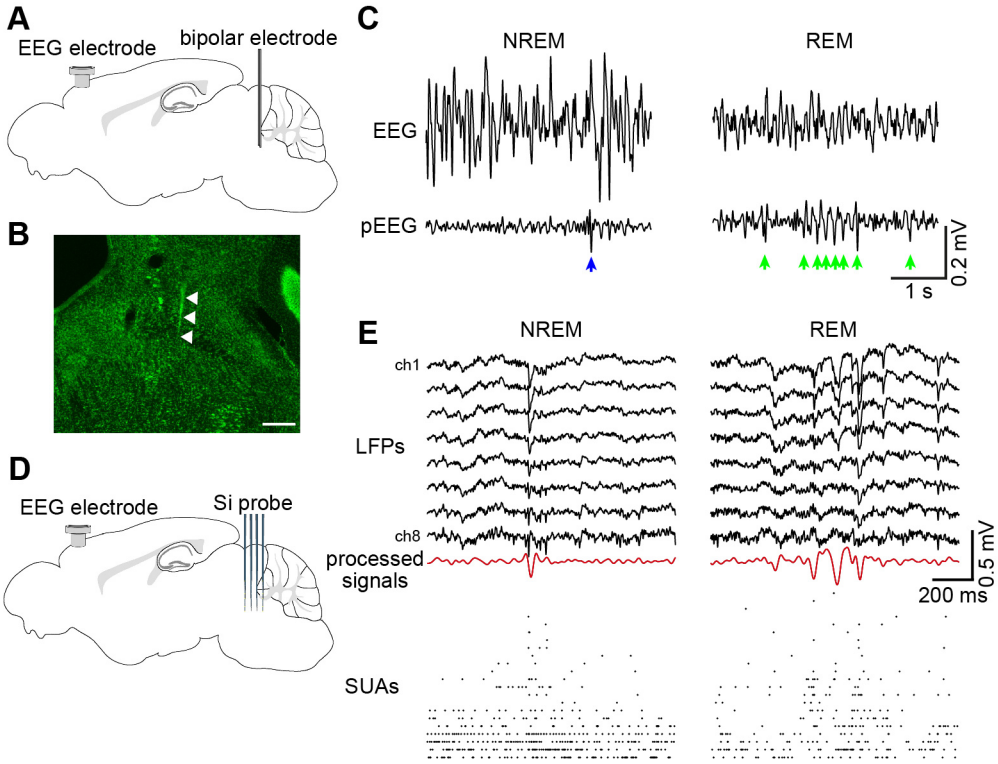

Figure 1. P-waves in mice.
(**A**) A diagram of the experimental approach for P-wave recording, showing a cortical EEG electrode and a bipolar electrode for pontine EEG recording in the mouse. A twisted bipolar electrode was also inserted to the neck muscle for EMG recording.
(**B**) A photograph, showing a track of a bipolar electrode in a mesopontine region. Scale bar, 500 μm.
(**C**) Examples of P-waves during NREM (*left*) and REM sleep (*right*).
(**D**) A diagram of the experimental approach for brainstem population recording, showing a cortical EEG electrode and a 32-channel silicon probe.
(**E**) Examples of local field potentials (LFPs) and simultaneously recorded single unit activities (SUAs) during NREM (*left*) and REM sleep (*right*). Processed LFP signals for P-wave detection (red) are also shown.

In all recording sessions where we could confirm REM sleep, we observed P-waves (**Figs. 1C and E**). The position of electrodes was histologically confirmed in the mesopontine region (**Fig. 1B**). P-waves often appeared as a cluster during REM sleep whereas P-waves during NREM sleep appeared less, typically in isolation (**Fig. 1C**). P-waves during both sleep states were accompanied by spiking activity across simultaneously recorded brainstem neurons (**Figs. 1E**), indicating that P-waves were locally generated neural events, rather than artifacts due to volume conduction or other sources. Thus, we could confirm P-waves in mice.

Establishment of a fully automated P-wave detection method

To quantify the property of P-waves, it is essential to detect P-waves objectively. To this end, we developed a signal processing workflow to detect P-waves in a fully automated fashion (**Fig. 2A**) (see Methods for more detail). **Figure 2B** shows example raw signals and processed signals with a

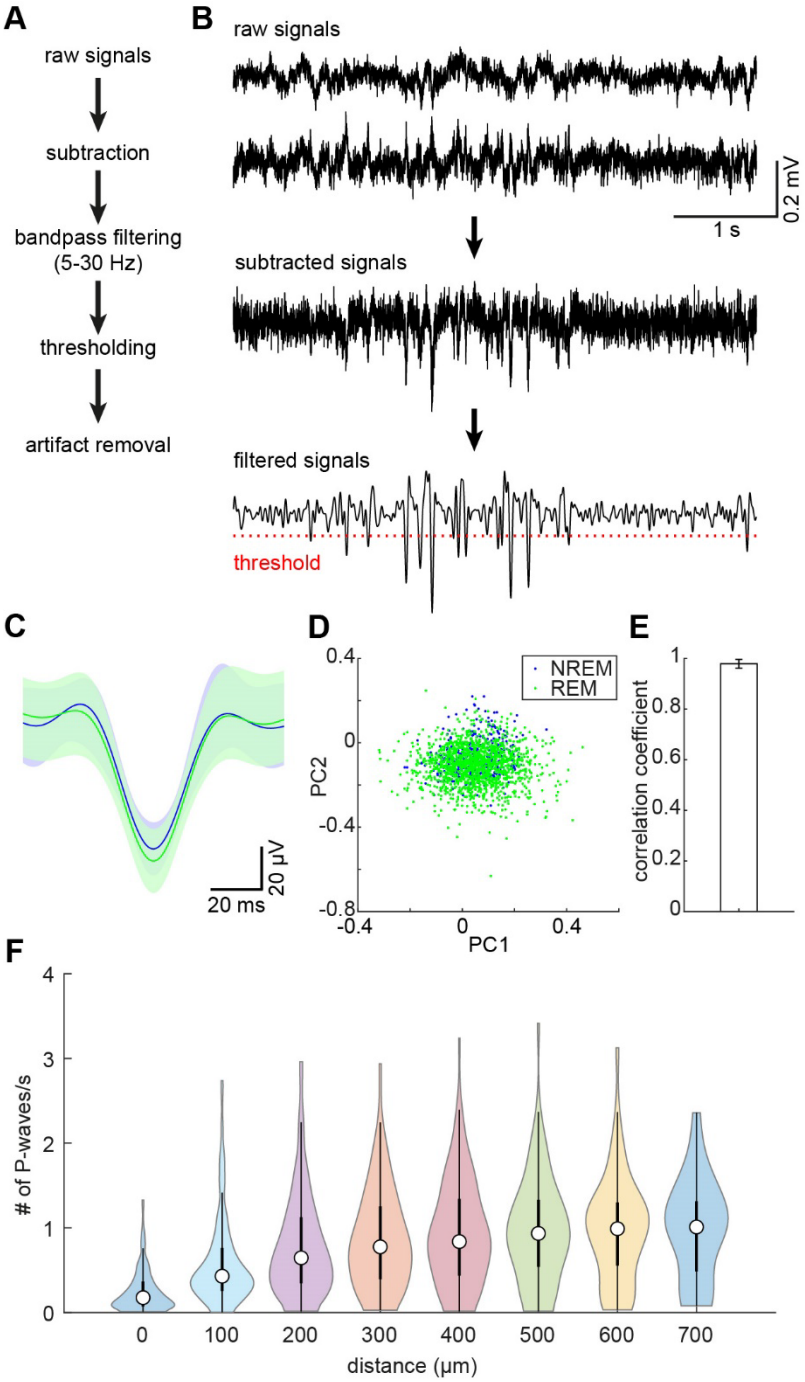

Figure 2. A P-wave detection method and the evaluation.
(**A**) An automated P-wave detection algorithm.
(**B**) Example traces of pontine EEGs.
(**C**) Average waveforms of P-waves. *blue*, P-waves during NREM sleep; *green*, P-waves during REM sleep. Errors indicate SD.
(**D**) Detected individual P-waves represented in first two principal component space.
(**E**) Comparisons of average waveforms of P-waves between sleep states based on Pearson's correlation coefficient (n = 16, r = 0.97 ± 0.01).
(**F**) Comparisons of the number of detected P-waves across different electrode distances. The effect of electrode distances was significant ($H_{(7)}$ = 257.4, p < 0.05, Kruskal-Wallis test).

detection threshold. The detection threshold was also automatically determined by signals during NREM sleep which provide a better estimate of the noise level since moving artifacts and P-waves appear less frequently compared to signals during other states. Our method allowed to detect P-waves across sleep states and datasets without any further optimization.

Since we also detected P-waves during NREM sleep, not just during REM sleep, we assessed whether detected P-waves were comparable between NREM sleep and REM sleep (**Figs. 2C-E**). As shown in **Figure 2C**, the average waveform of P-waves was similar between states. To quantify this tendency, we applied principal component analysis (PCA) (**Fig. 2D**) and measured Pearson's correlation coefficient (**Fig. 2E**). We confirmed the large overlap of individual waveforms between NREM and REM sleep in first 2 PC space (**Fig. 2D**) as well as high correlation coefficient (0.97 ± 0.01) (**Fig. 2E**), indicating that P-waves are quantitatively similar between sleep states.

In our bipolar electrode for P-wave monitoring, we intentionally separated the distance between two electrode tips vertically (~0.5 mm). Taking an advantage of a silicon probe with 100 μm spacing between two adjacent electrodes, we systematically assessed how electrode spacing affects the number of detected P-waves (**Fig. 2F**). Although the spacing was limited up to 700 μm, we confirmed a gradual increase in the number of detected P-waves up to around 500 μm. Less than 100 μm spacing significantly reduced the detectability of P-waves ($H_{(7)} = 257.4$, $p < 0.05$, Kruskal-Wallis test with *post-hoc* Dunn's test). In summary, we established a fully automated method to detect P-waves across sleep states together with showing the importance of the vertical spacing in electrodes.

Basic properties of P-waves in mice

By detecting P-waves across sleep states, we characterized properties of P-waves (**Fig. 3**). We began by comparing the frequency of P-waves between sleep states (**Fig. 3A**). The frequency of P-waves during REM sleep was around 0.5 – 1 Hz, and this was significantly higher than NREM sleep ($p < 0.0001$, rank sum test). We did not find any statistically significant difference in P-wave frequency between recording methods (bipolar electrodes v.s. silicon probes) ($p = 0.36$ during NREM; $p = 0.18$ during REM, rank sum test with Bonferroni correction).

Since P-waves during REM sleep often appeared as a cluster (**Fig. 1**), we quantified inter-event intervals (**Fig. 3B**). As expected, a large fraction of P-waves appeared within 200 ms especially during REM sleep. The median interval of P-waves was also significantly shorter during REM sleep (**Fig. 3B inset**) ($p < 0.0001$, rank sum test). To examine whether P-waves can appear synchronously in two hemispheres, we took the advantage of some datasets ($n = 9$ sessions from 5 animals) where bipolar electrodes were implanted in two hemispheres (**Fig. 3C**). Intriguingly, cross-correlation analysis showed a synchronous occurrence of P-waves between two hemispheres during both REM and NREM sleep. In addition, the cross-correlation profile during REM sleep exhibited a weak modulation at a 100 – 200 ms range, suggesting rhythmic theta synchrony between two hemispheres.

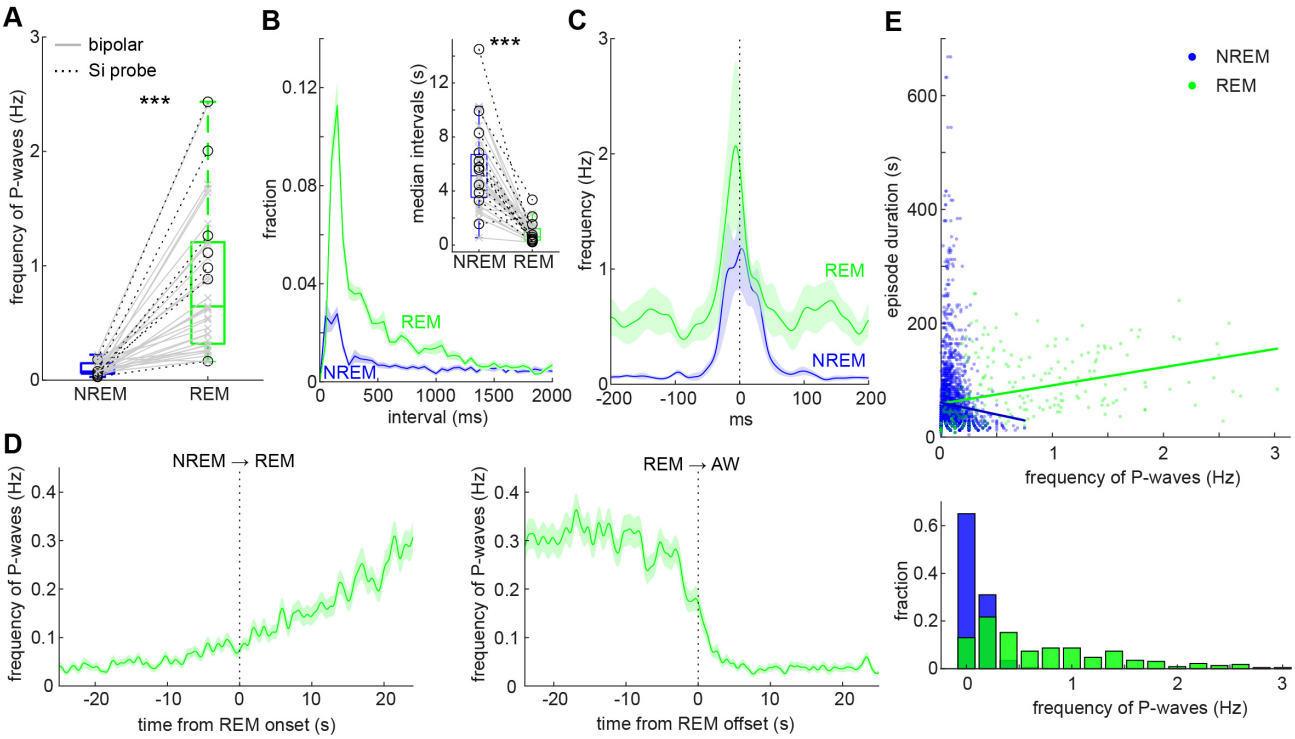

Figure 3. Features of P-waves in mice.
(**A**) Comparison of P-wave frequency between sleep states. *n* = 35 recordings. *** *p* <0.0001, rank sum test.
(**B**) Comparison of inter-event intervals between sleep states. inset, comparison of the medial intervals of P-waves between states. *n* = 35 recordings, *** *p* <0.0001, rank sum test.
(**C**) Cross-correlations of bilateral P-waves. *n* = 9 recordings.
(**D**) Temporal evolution of P-wave frequency around REM sleep onset (*left*) and offset (*right*). *n* = 99 REM sleep episodes.
(**E**) The relationship between P-wave frequency and sleep episode duration. Lines are linear regression lines. *Bottom*, distributions of P-wave frequency during NREM (blue) and REM sleep (green).

We further quantified how the frequency of P-waves changes around each REM sleep episode (**Fig. 3D**): more P-waves appeared just before REM sleep onset, their frequency gradually increased during REM sleep, and then it rapidly decreased around the termination of REM sleep episodes. Based on this observation, we wondered if the frequency of P-waves during REM sleep episode can correlate with the duration of REM sleep episode (**Fig. 3E**). We found that this is the case (r = 0.38, p < 0.0001) whereas the frequency of P-waves during NREM sleep negatively correlated with the episode duration (r = -0.064, p < 0.005). Altogether, these results reveal non-trivial properties of P-wave dynamics across sleep states.

Underlying brainstem neural activity during P-waves

While P-waves consist of a large deflection of LFPs (**Fig. 1**), it remains unclear whether underlying neural activity also consists of synchronous population firing or diverse neural activities. To address this issue, we analyzed single unit activity in the brainstem (**Fig. 4**). Indeed, many neurons exhibited the peak of their activity around P-wave timing (**Fig. 4A**). To examine whether the temporal structure of neural firing is preserved between NREM and REM sleep, we measured Pearson's correlation

coefficient between activity patterns in both states across neurons (**Fig. 4B**). Overall trend was significantly higher than zero ($p < 0.0001$, *t*-test). Thus, the firing pattern associated to P-waves was generally preserved across sleep states.

To assess the variability of neural firing patterns, we applied PCA to the activity profile during REM sleep (**Figs. 4C and D**). First 3 PCs explained >80% variability: PC1 and PC2 exhibited modulatory activity around P-wave timing (**Fig. 4D**). Consistent with this, most cells with showing peak activity around P-wave timing (black cells) were positive in the PC2 (**Fig. 4C**) whereas cells with showing peak activity after P-wave timing (red cells) generally appeared in the third and fourth quadrants (negative in PC2) (**Fig. 4C**). Thus, although many neurons fire around P-wave timing, P-waves comprise of variable neural ensembles.

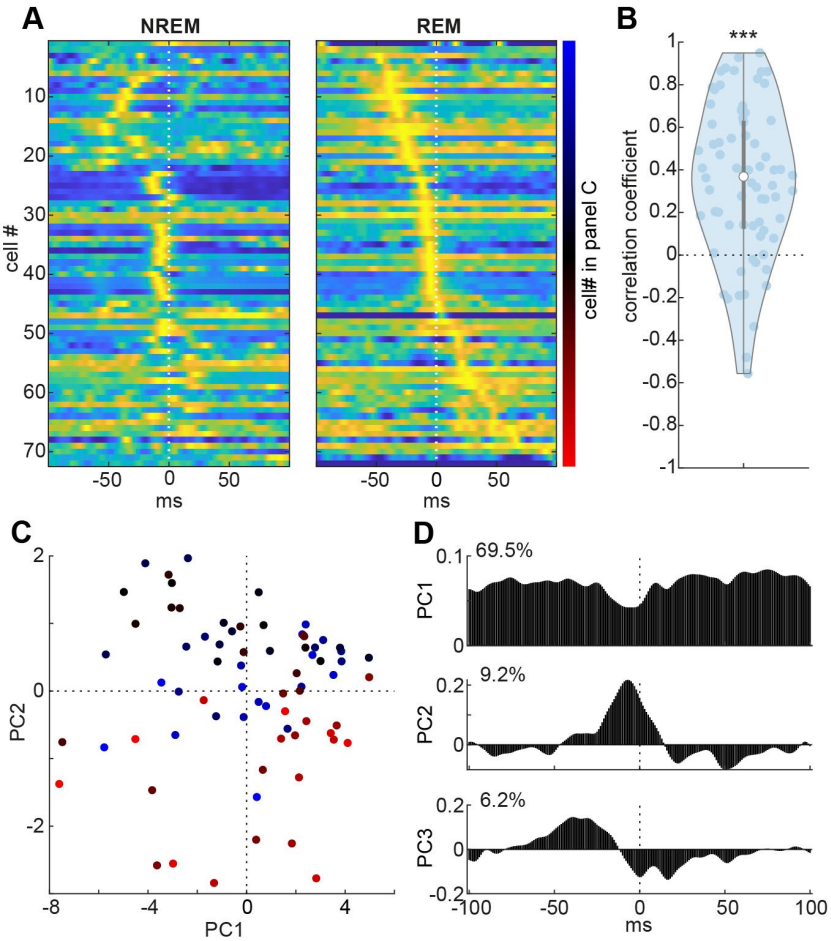

Figure 4. Brainstem neural firing during P-waves.
(**A**) Normalized average firing profiles across cells during NREM (*left*) and REM sleep (*right*). Cells were sorted by the peak timing during REM sleep. Color bar indicates cell numbers in panel (**C**).
(**B**) Comparisons of mean firing profiles between sleep states across cells based on Pearson's correlation coefficient. *** $p < 0.0001$, *t*-test.
(**C**) Mean firing profiles of individual neurons during REM sleep represented in first two PC space. Color indicates the order of the peak timing during REM sleep (A).
(**D**) First three PCs and explained variability.

Functional relationships between P-waves and SWRs during NREM sleep

Previously we demonstrated state-dependent functional coupling between P-waves and hippocampal oscillations across sleep states (Tsunematsu et al., 2020) and similar results were reported in macaque monkeys (Ramirez-Villegas et al., 2021). Here, we further examined if hippocampal sharp wave-ripples (SWRs) coupled with P-waves have distinct features and how P-waves can influence SWRs (**Fig. 5**). We began by comparing the frequency of SWRs and P-waves during NREM to REM sleep episodes (**Fig. 5B**). These two neural events appeared complementary:

although SWRs appeared mostly during NREM sleep, P-waves appeared more during REM sleep. During NREM sleep, more P-waves appeared immediately after SWRs (**Fig. 5C**) as reported previously (Tsunematsu et al., 2020), indicating that P-waves are coupled with SWRs.

Because SWRs plays a role in systems memory consolidation (Buzsaki, 2015, Fernandez-Ruiz et al., 2019, Jadhav et al., 2012),we wondered if P-waves during NREM sleep may also play a role. To gain an insight, we assessed whether P-waves can correlate with the modulation of power at the ripple frequency (140-250 Hz) (**Fig. 5D**). As expected from **Figure 5C**, ripple power steeply increased just before the timing of P-waves. However, ripple power rapidly decreased immediately after P-wave timing, implying that the occurrence of P-waves may lead to the termination of SWRs. To test this prediction, we compared the duration of SWRs depending on whether P-waves were coupled with SWRs in a short time window. Indeed, we found that SWRs coupled with P-waves within 30-ms window were significantly shorter than the remaining SWRs (**Fig. 5E**) ($p < 0.0001$, rank sum test). We further examined whether CA1 neural activity is modulated by P-waves. While a group

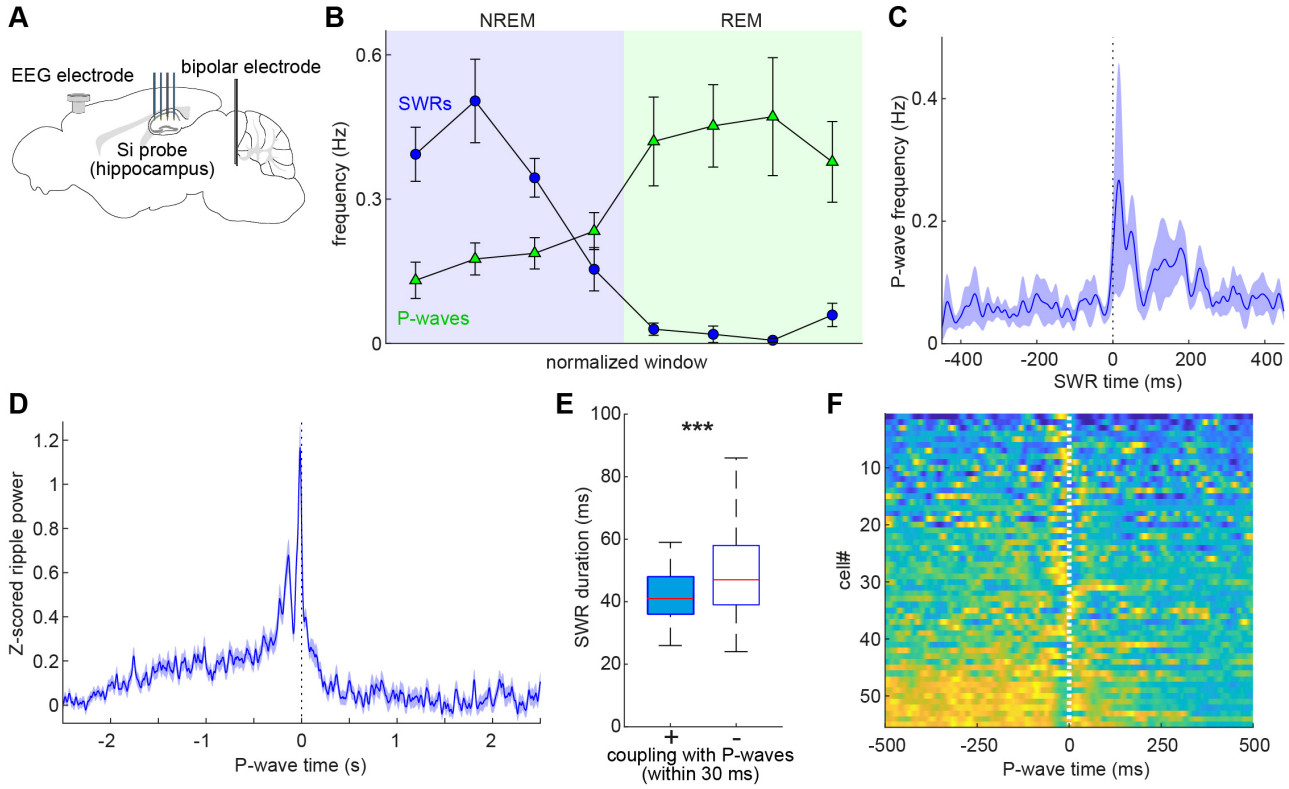

Figure 5. Functional coupling between P-waves and SWRs during NREM sleep.
(**A**) A diagram of the experimental approach for hippocampal population recording with pontine EEG monitoring, showing a cortical EEG electrode, a bipolar electrode for pontine EEG, a 32-channel silicon probe for hippocampal population recording.
(**B**) Temporal profiles of SWRs (blue) and P-waves across NREM and REM sleep episodes. Each episode duration was divided into four discrete time bins as normalized time windows.
(**C**) Cross-correlation between SWRs and P-waves during NREM sleep. $n = 4$ recordings.
(**D**) Cross-correlation between ripple (140-250 Hz) power profile and P-waves during NREM sleep. Each cross-correlation profile was z-scored based on the profile in -3~-2 sec window.
(**E**) Comparison of SWR duration between SWRs coupled with P-waves within 30 ms and other SWRs. *** $p < 0.0005$, rank sum test.
(**F**) Mean activity profiles of CA1 neurons relative to P-wave timing during NREM sleep. Cells were sorted by their first PC score.

of neurons showed strong modulation at around the timing of P-waves, a subset of neurons exhibited the reduction in their firing after P-waves (**Fig. 5F**). These results suggest that although P-waves are functionally coupled with hippocampal SWRs, P-waves play an antagonistic role in SWRs.

Functional coupling between P-waves and hippocampal theta oscillations during REM sleep

Finally, we examined how P-waves are coupled with hippocampal theta oscillations during REM sleep and how P-waves is associated with the modulation of CA1 neuronal excitability (**Fig. 6**). Firstly, we computed the average of hippocampal LFPs triggered by P-wave onsets (**Fig. 6A**). As expected, the average profile showed rhythmic modulation around P-wave onset. We assessed this in the frequency domain by applying a wavelet transformation (**Fig. 6B**). We confirmed that this modulation was at theta (7-10 Hz) frequency. We also determined when P-wave appeared during each theta cycle (**Fig. 6C**). More P-waves appeared at a rising phase of theta oscillation ($p < 0.0001$, Rayleigh test for non-uniformity). These results reassured that P-waves were phase-coupled with hippocampal theta oscillations during REM sleep.

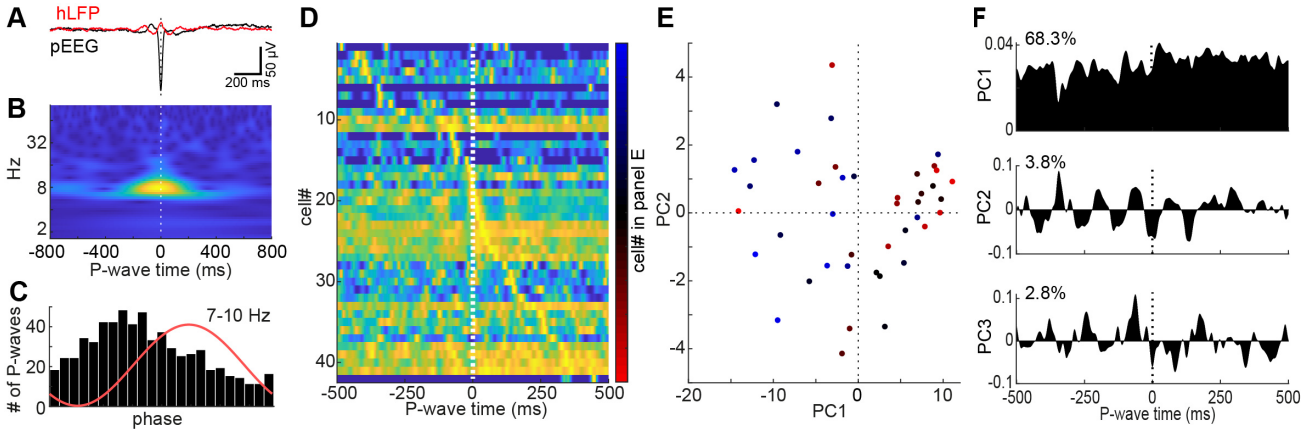

Figure 6. Functional coupling between P-waves and hippocampal activity during REM sleep.
(**A**) The average hippocampal LFPs triggered by P-wave timing.
(**B**) A scalogram of P-wave-triggered hippocampal LFPs.
(**C**) A phase diagram of P-wave timing relative to hippocampal theta rhythms.
(**D**) Normalized average firing profiles across CA1 neurons relative to P-wave timing during REM sleep. Cells were sorted by the peak timing. Color bar indicates cell numbers in panel (**E**).
(**E**) Mean firing profiles of individual CA1 neurons relative to P-wave timing represented in first two PC space. Color indicates the order of the peak timing (D).
(**F**) First three PCs and explained variability.

We further examined whether and how P-waves modulate hippocampal individual neuronal activity by analyzing single unit activity in CA1 (**Figs. 6D-F**). As previously reported (Tsunematsu et al., 2020), a subset of CA1 neurons exhibited strong activity immediately after P-wave onset (**Fig. 6D**). In addition, we noticed diverse activity in CA1 populations around P-waves. To quantify this trend, we applied PCA (**Figs. 6E and F**). First three PCs explained >70% variance: the first PC captured the profile that activity slightly increases after P-waves whereas the second PC exhibited that strong

theta-modulated activity becomes weaker 200~350 ms after P-waves. The third PC also captured a similar asymmetric profile of theta modulations. In the first two PC space, a group of CA1 neurons showed high positive values in PC1, indicating an increase in their firing after P-waves (**Fig. 6E**). On the other hand, a small fraction of CA1 neurons showed high positive (~4) or negative scores (~-4) in PC2, indicating changes in their theta-modulations (**Fig. 6E**). These results indicate that while P-waves are phase-coupled with hippocampal theta rhythm, P-waves can also lead to modulated excitability in CA1 neurons.

Discussion

Although P-waves have long been recognized as a prominent electrophysiological marker of REM sleep, the detailed characteristics and functional significance of P-waves remains poorly understood. Here, by performing multiple types of *in vivo* electrophysiological experiments in mice and establishing a fully automated detection method of P-waves, we reported detailed electrophysiological properties of P-waves in mice for the first time. In addition, we reported non-trivial state-dependent modulatory effects of P-waves on hippocampal excitability: an antagonistic coupling between P-waves and SWRs during NREM sleep, and theta-P-wave coupling leading to the modulation of CA1 excitability during REM sleep. These results indicate that P-waves are part of brain-wide neural ensembles during sleep, suggesting the functional importance of P-waves.

Comparisons with previous studies

P/PGO waves have been described in multiple mammalian species, including cats (Bizzi and Brooks, 1963a, Brooks and Bizzi, 1963, Datta, 1997, Jouvet et al., 1959), macaques (Cohen and Feldman, 1968, Ramirez-Villegas et al., 2021), rats (Farber et al., 1980) and humans (Lim et al., 2007). However, the existence of P-waves in mice has been anecdotal despite the importance of the animal model. Recently, we showed P-waves in mice directly by using electrophysiological methods and indirectly by applying fiber photometry (Patel et al., 2020, Tsunematsu et al., 2020). In the present study, we analyzed the same datasets, with additional new datasets where simultaneous P-wave monitoring from two hemispheres. To the best of our knowledge, except our resent study (Tsunematsu et al., 2020), this is for the first time to investigate brainstem neural population activity underlying P-waves and state-dependent functional coupling between P-waves and hippocampal oscillations by monitoring hippocampal population activity at the single-cell level.

P-waves in mice are similar to those in other species, with respect to the following features. Firstly, the waveform of P-waves in mice (**Figs. 1C and 2C**) is similar to that in other species (Datta, 1997). We quantitatively confirmed that the waveform of P-waves is comparable between REM and NREM sleep. Secondly, the characteristics of P-waves in mice are also comparable with those in other species (Datta, 1997), with respect to higher frequency of P-waves during REM sleep and a gradual increase in P-wave frequency around REM sleep onset.

In addition to these, we confirmed that P-waves are functionally coupled with SWRs and theta oscillations. A similar functional coupling between the hippocampus and cerebellum has been reported recently (Torres-Herraez et al., 2022) although it remains to be confirmed if the neural events in the cerebellum are P-waves or not. More importantly, even macaque monkeys exhibit similar functional coupling (Ramirez-Villegas et al., 2021). These results suggest that P/PGO waves are part of brain-wide neural ensembles across sleep states. In the present study, we reported three

non-trivial observations: firstly, P-waves appear synchronously in both hemispheres, implying an induction mechanism of P-waves (see below). Secondly, although P-waves are functionally coupled with SWRs during NREM sleep, the occurrence of P-waves was associated with the reduction in ripple power as well as CA1 neural firing. Finally, during REM sleep, P-waves led to the modulation of excitability of CA1 populations, not just the coupling of P-waves with theta rhythms. To the best of our knowledge, this is the first to demonstrate sleep state-dependent effects of P-waves on hippocampal activity.

Possible mechanisms of P-wave genesis

Mesopontine cholinergic neurons have long been implicated in the induction of P/PGO waves (Datta, 1995, Datta, 1997). Recently, by expressing genetically encoded calcium indicators in cholinergic neurons, we confirmed that mesopontine cholinergic activity is phase-locked to the onset of P-waves (Patel et al., 2020). In the present study, we showed that brainstem neural ensembles consist of diverse functional classes while activity patterns are generally consistent between sleep states. Our results suggest that although the induction mechanism of P-waves is generally similar between sleep states, the frequency of P-waves may be influenced by global brain-wide activities across sleep states. In addition, P-waves appeared in two hemispheres synchronously. Although we do not exclude the possibility that P-waves are generated in one hemisphere first, then P-waves start to synchronize in both hemispheres, our observation provides an important implication for the mechanism of P-wave genesis. Because a subset of mesopontine cholinergic neurons form commissural projections (Mena-Segovia and Bolam, 2017), these neurons may play a role in the synchronization of P-waves between two hemispheres. It would be important to investigate detailed anatomical and synaptic connections within the mesopontine region between hemispheres in the future.

Functional implications of P-waves

What are functional consequences of state-dependent coupling of P-waves with hippocampal oscillations? Because both SWRs and theta oscillations have been implicated in systems memory consolidation (Buzsaki, 2015, Fernandez-Ruiz et al., 2019, Jadhav et al., 2012, Boyce et al., 2016), P-waves may also play a role in memory consolidation. However, given our findings (**Figs. 5 and 6**), the role of P-waves may also be state-dependent.

Recently it has been shown that the duration of SWRs causally link the degree of memory consolidation (Fernandez-Ruiz et al., 2019). Because we showed that SWRs coupled with P-waves are shorter than other SWRs, P-waves during NREM sleep may play a modulatory role to avoid excessive activations of hippocampal populations. It remains to be determined how P-waves during

NREM sleep can affect downstream activity and how experience before sleep episodes can affect this unexpected, antagonistic interaction between SWRs and P-waves.

Although an exact role of REM sleep in systems memory consolidation remains controversial (Poe, 2017, Sara, 2017), theta oscillations during REM sleep play a causal role in memory consolidation (Boyce et al., 2016) and pharmacological manipulations of P-waves affect memory consolidation (Datta et al., 2004). While it has long been known that P-waves are phase-coupled with ongoing theta oscillations (Karashima et al., 2002, Karashima et al., 2004, Karashima et al., 2005, Ramirez-Villegas et al., 2021, Sakai et al., 1973, Tsunematsu et al., 2020), our results showed that P-waves can also modulate the excitability in the hippocampus. Because REM sleep can reorganize hippocampal population activity (Grosmark et al., 2012), it would be interesting to see how P-waves can contribute to such a reorganization of hippocampal excitability and whether manipulations of P-waves can affect it.

Limitations of the study

Although our results provide insight into the functional significance of P-waves, the present study has limitations in the following aspects: firstly, determining exact cell-types of recorded neurons in the brainstem was challenging. This can be refined by adopting state-of-the-art Neuropixels probe technology with an advanced histological analysis, and/or cell-type-specific activity monitoring with genetically encoded indicators. Secondly, although we characterized state-dependent coupling between P-waves and hippocampal oscillations, it would be important to directly determine the functional role of these coupling by manipulating P-waves while mice perform a behavioral task before and after sleep. Despite these limitations, however, our results provide a basis for future studies toward a better understanding of the regulatory mechanisms and functions of P-waves and sleep states.

Conclusions

While P-waves appear synchronously in both hemispheres during both NREM and REM sleep, the frequency of P-waves differs between states. Underlying neural ensembles are generally consistent between states, suggesting a similar local induction mechanism. Because functional coupling between P-waves and hippocampal oscillations differ between sleep states, P-waves may contribute to brain-wide neural ensembles in a state-dependent fashion. In addition, state-dependent coupling of P-waves and hippocampal oscillations may lead to distinct consequences in their downstream neural circuits. Thus, these state-dependent coordinated activities may realize distinct functions of sleep states.

Methods

Animals

17 male mice (8-26 week old) were used in this study and were housed individually with a 12 h:12 h light/dark cycle (light on hours: 7:00-19:00 for 15 mice, 8:00-20:00 for 2 mice). Mice had *ad libitum* access to food and water. Their genotypes consisted of wild-type, ChAT-IRES-Cre (JAX006410), or ChAT-IRES-Cre::Ai32 (JAX012569) on C57BL/6 background. For brainstem silicon probe recordings, 7 animals were used (9 recordings). For hippocampal silicon probe recordings, 2 animals were used (4 recordings). For P-wave recordings with bipolar electrodes, 8 animals were used (15 recording sessions with 9 bilateral recordings). All experiments were performed during the light period (zeitgeber time (ZT) 1-6). All experimental procedures were performed in accordance with the United Kingdom Animals (Scientific Procedures) Act of 1986 Home Office regulations and approved by the Home Office (PPL 70/8883) and the Animal Care and Use Committee of Tohoku University (approval no. 2019LsA-018).

Surgical procedures

Detailed procedures were described elsewhere (Tsunematsu et al., 2020). Briefly, mice were anesthetized with isoflurane (2-5% for induction, 1-2% for maintenance) and placed in a stereotaxic apparatus (SR-5M-HT or SR-6M-HT, Narishige). Body temperature was maintained at 37°C with a feedback temperature controller (40–90–8C, FHC). After exposing the skull, two bone screws were implanted on the skull for cortical EEGs. Twisted wires (AS633, Cooner Wire) were inserted into the neck muscle for EMG. For pontine EEG recording, bipolar electrodes for pontine EEGs were typically implanted in the medial parabrachial nucleus of the pons (5.1 mm posterior, 1.2 mm lateral from bregma, 3.2 mm depth from brain surface). The bipolar electrodes consisted of 75 or 100 μm diameter stainless wires (FE631309, Advent Research Materials; FE205850, Goodfellow; EKCSS-010, Bio Research Center). The tip of two glued wires were separated by approximately 0.5 mm vertically to differentiate signals. A pair of nuts was also attached on the skull with dental cement as a head-post. After the surgery, Carprofen (Rimadyl, 5 mg/kg) was administered intraperitoneally. The animals were left to recover for at least 5 days. During the habituation period, the animals were placed in a head-fixed apparatus, by securing them by the head-post and placing the animal into an acrylic tube. This procedure was continued for at least 5 days, during which the duration of head-fixed was gradually extended from 10 to 120 min. After this period, recording was performed for up to 5 hours (see below).

For silicon probe recording, in addition to the procedures above, a day after the habituation period, the animals were anesthetized with isoflurane and a craniotomy to insert silicon probe the brainstem or hippocampus was performed. A craniotomy on the left hemisphere (4.0 mm to 5.5 mm posterior, 1.0 to 1.3 mm lateral from bregma) for the brainstem recording and on the left hemisphere (2.0 mm

posterior, 1.5 mm lateral from bregma) for the hippocampus recording were performed, respectively. To protect and prevent the brain from drying, the surface was covered with biocompatible sealants (Kwik-Sil and Kwik-Cast, WPI). The following day, the animals were placed in the head-fixed apparatus for silicon probe recording.

in vivo electrophysiological recording

Electrophysiological recordings were performed in a single-walled acoustic chamber (MAC-3, IAC Acoustics) with the interior covered with 3 inches of acoustic absorption foam. The animals were placed in the same head-fixed apparatus, by securing them by the head-post and placing the animal into an acrylic tube. During the entire recording, the animals were not required to do anything actively. For pontine EEG recording, cortical EEG, EMG and pontine EEG signals were amplified (HST/32V-G20 and PBX3, Plexon), filtered (0.1 Hz low cut), digitized at a sampling rate of 1 kHz and recorded using LabVIEW software (National Instruments). A subset of recordings was performed by using an Intan Technologies system (RHD 16-channel bipolar-input recording headstage, RHD2000). Recording was performed for approximately 5 hrs between ZT1-6.

For silicon probe recording, a 32 channels 4 shank silicon probe (A4 x 8-5 mm-100-400-177 for brainstem recording or Buzsaki32 for hippocampus recording) was inserted slowly with a manual micromanipulator (SM-25A, Narishige) into the brainstem (3.75 mm – 4.3 mm from the brain surface) or the hippocampus (1.55 mm – 1.85 mm from brain surface). Broadband signals were amplified (HST/32V-G20 and PBX3, Plexon) relative to screw on the cerebellum, filtered (0.1 Hz low cut), digitized at 20 kHz and recorded using LabVIEW software (National Instruments). The recording session was initiated > 1 hr after the probe was inserted to its target depth, to stabilize neural signals. For verification of silicon probe tracks, the rear of the probes were painted with DiI (~10% in ethanol, D282, Invitrogen) before insertion. Pupillometry was also measured simultaneously from a subset of recordings. The experimental procedures and results of pupillometry were reported elsewhere (Tsunematsu et al., 2020).

Histological analysis

After electrophysiological experiments, animals were deeply anesthetized with mixture of pentobarbital and lidocaine and perfused transcardially with saline or phosphate buffer saline (PBS) followed by 4% paraformaldehyde/0.1 M phosphate buffer, pH 7.4. The brains were removed and immersed in the above fixative solution overnight at 4°C and then immersed in a 30% sucrose in PBS for at least 2 days. The brains were cut into coronal or sagittal sections with a sliding microtome (SM2010R, Leica) or with a cryostat (CM3050, Leica) with a thickness of 50 or 100 μm. To identify the location of electrode positions, the brain sections were incubated with a NeuroTrace 500/525 Green-Fluorescence (1/350, Invitrogen) or NeuroTrace 435/455 Blue-Fluorescence (1/100,

Invitrogen) in PBS for 20 min at room temperature (RT). After staining, sections were mounted on gelatin-coated or MAS-coated slides and cover-slipped with 50% glycerol in PBS. The sections were examined with a fluorescence microscope (BZ-9000, Keyence).

Data analysis

Sleep scoring

Vigilance states were visually scored offline according to standard criteria as described elsewhere (Patel et al., 2020, Tsunematsu et al., 2020). Wakefulness, NREM sleep, or REM sleep was determined in every 4 second based on cortical EEG and EMG signals using custom-made MATLAB GUI (https://github.com/Sakata-Lab/SleepScore) or SleepSign (KISSEI COMTEC).

P-wave detection

To detect P-waves, two EEG or LFP signals in the pons were subtracted and filtered (5-30 Hz band-pass filter). If the signals cross a threshold, the event was recognized as candidates of P-waves. To determine the detection threshold, a segment of signals was extracted from the longest NREM sleep episode for a reliable estimation of the noise level. The noise level was estimated by computing root-mean-square (RMS) values in every 10 ms window. The threshold was defined as mean + 5 x standard deviation of the RMS values. To eliminate potential moving artifacts, EMG signals were also assessed in parallel. If the RMS values of EMG signals cross a threshold, the candidate was discarded. The threshold was defined as mean + 3 × standard deviation (SD) of the RMS values of EMG signals with 10 ms resolution. The timing of P-waves was defined as the timing of the negative peak. To assess how the distance between two electrodes affects the performance of P-wave detection (**Fig. 2F**), pairs of electrodes in each silicon probe shank were systematically chosen. LFPs from these electrodes were processed as described above.

Spike train and hippocampal LFP analysis

For spike sorting, Kilosort (Pachitariu et al., 2016) was used for automatic processing, followed by manual curation using phy (https://github.com/cortex-lab/phy). Clusters with ≥ 20 isolation distance were recognized as single units. The position of single units was estimated based on the channel providing the largest spike amplitude. All subsequent analysis was performed using custom-written codes (MATLAB, Mathworks). For principal component analysis, MATLAB *pca* function was used after normalizing average spiking activity by the peak firing rate.

To detect ripples in the hippocampus, LFP signals were band-pass filtered at 140-250 Hz with 3rd-order butterworth filter. The envelope of the filtered signals was calculated by computing root-mean-square values using a sliding window of 20-ms data points. The mean and SD of this “ripple” power profile were used to compute two thresholds (mean + 5×SD and mean + 2×SD), which were used to

detect SWRs and to determine their onset, peak timing and offset. To detect SWRs, the period of the ripple power larger than the threshold (mean + 5×SD) was recognized as SWR candidates. The peak timing of each candidate was defined as SWR timing. The onset and offset of each candidate were determined as time points when the candidate power profile crossed the threshold (mean + 2×SD). If the onset and offset were overlapped across multiple SWR candidates, they were merged as a single SWR and the SWR timing was defined as the time point providing the maximum power. Finally, the candidate shorter than 20 ms or longer than 200 ms were excluded. This process was applied to all silicon probe channels. Signals from the channel which provided the maximum frequency of SWRs during NREM sleep, but low frequency of SWRs during REM sleep was used.

The phase analysis (**Fig. 6C**) was the same as that described previously (Tsunematsu et al., 2020, Yague et al., 2017). LFP signals from two separate channels were subtracted to minimize volume conduction. To derive band-limited signals at theta band (7 – 10 Hz), a Kaiser finite impulse response filter with sharp transition bandwidth of 1 Hz, pass-band ripple of 0.01 dB and stop-band attenuation of 50 dB. For filtering, MATLAB *filtfilt* function was used. The instantaneous phase of theta band was estimated from the Hilbert transform and the phase of P-wave occurrence was computed. To quantify the relationship between P-waves and LFP phase, the number of P-waves elicited in each phase bin was calculated. The resultant vector length was computed as an absolute value of mean resultant vector *r* by using *circ_r* function of CircStats Toolbox (Berens, 2009). Rayleigh's test for non-uniformity of circular data was performed to assess the statistical significance ($p < 0.01$) of the non-uniformity of the P-wave vs LFP phase distribution.

Statistical analysis

Data was presented as mean ± SEM unless otherwise stated. Statistical analyses were performed with MATLAB (version R2021a). In **Figure 2F**, Kruskal-Wallis test with *post-hoc* Dunn's test was performed. In **Figures 3A, 3B** and **5E**, Wilcoxon rank sum test was performed. In **Figure 3E**, Pearson's cross-correlation analysis was performed. In **Figure 4B**, Student's *t*-test was performed.

Acknowledgements

We thank Dr Tomomi Sanagi for technical assistance and Dr Mirna Merkler and Ms Erin Moran for proofreading. This work was supported by Leverhulme Trust (RPG-2015-377), MRC (MR/V033964/1) and Horizon2020-RIA (DEEPER, 101016787) to SS, and the Japan Society for the Promotion of Science (JSPS) Postdoctoral Fellow for Research Abroad, a Research Fellowship from the Uehara Memorial Foundation, FOREST (JPMJFR2047) from Japan Science and Technology Agency and by JSPS KAKENHI (20H05047) to TT.

Author contributions

TT and SM performed all *in vivo* electrophysiological experiments and associated histological analysis and sleep scoring. SS performed all other data analysis. SS wrote the manuscript with inputs from TT and SM.

References

Adamantidis, A. R., Gutierrez Herrera, C. & Gent, T. C. 2019. Oscillating circuitries in the sleeping brain. *Nat Rev Neurosci,* 20**,** 746-762.

Berens, P. 2009. CircStat: A Matlab Toolbox for Circular Statistics. *Journal of statistical software,* 31**,** 1-21.

Bizzi, E. & Brooks, D. C. 1963a. Functional Connections between Pontine Reticular Formation and Lateral Geniculate Nucleus during Deep Sleep. *Arch Ital Biol,* 101**,** 666-80.

Bizzi, E. & Brooks, D. C. 1963b. Pontine reticular formation: relation to lateral geniculate nucleus during deep sleep. *Science,* 141**,** 270-2.

Boyce, R., Glasgow, S. D., Williams, S. & Adamantidis, A. 2016. Causal evidence for the role of REM sleep theta rhythm in contextual memory consolidation. *Science,* 352**,** 812-6.

Brooks, D. C. & Bizzi, E. 1963. Brain Stem Electrical Activity during Deep Sleep. *Arch Ital Biol,* 101**,** 648-65.

Brown, R. E., Basheer, R., Mckenna, J. T., Strecker, R. E. & Mccarley, R. W. 2012. Control of sleep and wakefulness. *Physiol Rev,* 92**,** 1087-187.

Buzsaki, G. 2015. Hippocampal sharp wave-ripple: A cognitive biomarker for episodic memory and planning. *Hippocampus,* 25**,** 1073-188.

Byron, N., Semenova, A. & Sakata, S. 2021. Mutual Interactions between Brain States and Alzheimer's Disease Pathology: A Focus on Gamma and Slow Oscillations. *Biology (Basel),* 10.

Callaway, C. W., Lydic, R., Baghdoyan, H. A. & Hobson, J. A. 1987. Pontogeniculooccipital waves: spontaneous visual system activity during rapid eye movement sleep. *Cell Mol Neurobiol,* 7**,** 105-49.

Calvo, J. M. & Fernandez-Guardiola, A. 1984. Phasic activity of the basolateral amygdala, cingulate gyrus, and hippocampus during REM sleep in the cat. *Sleep,* 7**,** 202-10.

Cohen, B. & Feldman, M. 1968. Relationship of electrical activity in pontine reticular formation and lateral geniculate body to rapid eye movements. *J Neurophysiol,* 31**,** 806-17.

Datta, S. 1995. Neuronal activity in the peribrachial area: relationship to behavioral state control. *Neurosci Biobehav Rev,* 19**,** 67-84.

Datta, S. 1997. Cellular basis of pontine ponto-geniculo-occipital wave generation and modulation. *Cell Mol Neurobiol,* 17**,** 341-65.

Datta, S. 2012. Phasic Pontine-Wave (P-Wave) Generation: Cellular-Molecular-Network Mechanism and Functional Significance. *In:* FRANK, M. G. (ed.) *Sleep and Brain Activity.* San Diego: Academic Press.

Datta, S., Mavanji, V., Ulloor, J. & Patterson, E. H. 2004. Activation of phasic pontine-wave generator prevents rapid eye movement sleep deprivation-induced learning impairment in the rat: a mechanism for sleep-dependent plasticity. *J Neurosci,* 24**,** 1416-27.

Datta, S., Siwek, D. F., Patterson, E. H. & Cipolloni, P. B. 1998. Localization of pontine PGO wave generation sites and their anatomical projections in the rat. *Synapse,* 30**,** 409-23.

Farber, J., Marks, G. A. & Roffwarg, H. P. 1980. Rapid eye movement sleep PGO-type waves are present in the dorsal pons of the albino rat. *Science,* 209**,** 615-7.

Fernandez-Ruiz, A., Oliva, A., Fermino De Oliveira, E., Rocha-Almeida, F., Tingley, D. & Buzsaki, G. 2019. Long-duration hippocampal sharp wave ripples improve memory. *Science,* 364**,** 1082-1086.

Grosmark, A. D., Mizuseki, K., Pastalkova, E., Diba, K. & Buzsaki, G. 2012. REM sleep reorganizes hippocampal excitability. *Neuron,* 75**,** 1001-7.

Herice, C., Patel, A. A. & Sakata, S. 2019. Circuit mechanisms and computational models of REM sleep. *Neurosci Res,* 140**,** 77-92.

Jadhav, S. P., Kemere, C., German, P. W. & Frank, L. M. 2012. Awake hippocampal sharp-wave ripples support spatial memory. *Science,* 336**,** 1454-8.

Jouvet, M., Jeannerod, M. & Delorme, F. 1965. [Organization of the system responsible for phase activity during paradoxal sleep]. *C R Seances Soc Biol Fil,* 159**,** 1599-604.

Jouvet, M., Michel, F. & Courjon, J. 1959. [Electric activity of the rhinencephalon during sleep in cats]. *C R Seances Soc Biol Fil,* 153**,** 101-5.

Karashima, A., Nakamura, K., Sato, N., Nakao, M., Katayama, N. & Yamamoto, M. 2002. Phase-locking of spontaneous and elicited ponto-geniculo-occipital waves is associated with acceleration of hippocampal theta waves during rapid eye movement sleep in cats. *Brain Res,* 958**,** 347-58.

Karashima, A., Nakao, M., Honda, K., Iwasaki, N., Katayama, N. & Yamamoto, M. 2004. Theta wave amplitude and frequency are differentially correlated with pontine waves and rapid eye movements during REM sleep in rats. *Neurosci Res,* 50**,** 283-9.

Karashima, A., Nakao, M., Katayama, N. & Honda, K. 2005. Instantaneous acceleration and amplification of hippocampal theta wave coincident with phasic pontine activities during REM sleep. *Brain Res,* 1051**,** 50-6.

Lim, A. S., Lozano, A. M., Moro, E., Hamani, C., Hutchison, W. D., Dostrovsky, J. O., Lang, A. E., Wennberg, R. A. & Murray, B. J. 2007. Characterization of REM-sleep associated ponto-geniculo-occipital waves in the human pons. *Sleep,* 30**,** 823-7.

Lu, J., Sherman, D., Devor, M. & Saper, C. B. 2006. A putative flip-flop switch for control of REM sleep. *Nature,* 441**,** 589-94.

Luppi, P. H., Gervasoni, D., Verret, L., Goutagny, R., Peyron, C., Salvert, D., Leger, L. & Fort, P. 2006. Paradoxical (REM) sleep genesis: the switch from an aminergic-cholinergic to a GABAergic-glutamatergic hypothesis. *J Physiol Paris,* 100**,** 271-83.

Mccarley, R. W. 2007. Neurobiology of REM and NREM sleep. *Sleep Med,* 8**,** 302-30.

Mena-Segovia, J. & Bolam, J. P. 2017. Rethinking the Pedunculopontine Nucleus: From Cellular Organization to Function. *Neuron,* 94**,** 7-18.

Pachitariu, M., Steinmetz, N., Kadir, S., Carandini, M. & Harris, K. D. 2016. Kilosort: realtime spike-sorting for extracellular electrophysiology with hundreds of channels. *BioRxiv***,** 061481.

Patel, A. A., Mcalinden, N., Mathieson, K. & Sakata, S. 2020. Simultaneous Electrophysiology and Fiber Photometry in Freely Behaving Mice. *Front Neurosci,* 14**,** 148.

Poe, G. R. 2017. Sleep Is for Forgetting. *J Neurosci,* 37**,** 464-473.

Ramirez-Villegas, J. F., Besserve, M., Murayama, Y., Evrard, H. C., Oeltermann, A. & Logothetis, N. K. 2021. Coupling of hippocampal theta and ripples with pontogeniculooccipital waves. *Nature,* 589**,** 96-102.

Sakai, K., Sano, K. & Iwahara, S. 1973. Eye movements and hipocampal theta activity in cats. *Electroencephalogr Clin Neurophysiol,* 34**,** 547-9.

Sara, S. J. 2017. Sleep to Remember. *J Neurosci,* 37**,** 457-463.

Steriade, M. 2006. Grouping of brain rhythms in corticothalamic systems. *Neuroscience,* 137**,** 1087-106.

Steriade, M., Mccormick, D. A. & Sejnowski, T. J. 1993. Thalamocortical oscillations in the sleeping and aroused brain. *Science,* 262**,** 679-85.

Torres-Herraez, A., Watson, T. C. & Rondi-Reig, L. 2022. Delta oscillations coordinate intra-cerebellar and cerebello-hippocampal network dynamics during sleep. *J Neurosci*.

Tsunematsu, T., Patel, A. A., Onken, A. & Sakata, S. 2020. State-dependent brainstem ensemble dynamics and their interactions with hippocampus across sleep states. *Elife,* 9.

Van Dort, C. J., Zachs, D. P., Kenny, J. D., Zheng, S., Goldblum, R. R., Gelwan, N. A., Ramos, D. M., Nolan, M. A., Wang, K., Weng, F. J., Lin, Y., Wilson, M. A. & Brown, E. N. 2015. Optogenetic activation of cholinergic neurons in the PPT or LDT induces REM sleep. *Proc Natl Acad Sci U S A,* 112**,** 584-9.

Yague, J. G., Tsunematsu, T. & Sakata, S. 2017. Distinct Temporal Coordination of Spontaneous Population Activity between Basal Forebrain and Auditory Cortex. *Front Neural Circuits,* 11**,** 64.

Figure Legends

Figure 1. P-waves in mice.

(**A**) A diagram of the experimental approach for P-wave recording, showing a cortical EEG electrode and a bipolar electrode for pontine EEG recording in the mouse. A twisted bipolar electrode was also inserted to the neck muscle for EMG recording.

(**B**) A photograph, showing a track of a bipolar electrode in mesopontine region. Scale bar, 500 μm.

(**C**) Examples of P-waves during NREM (left) and REM sleep (right).

(**D**) A diagram of the experimental approach for brainstem population recording, showing a cortical EEG electrode and a 32-channel silicon probe.

(**E**) Examples of local field potentials (LFPs) and simultaneously recorded single unit activities (SUAs) during NREM (left) and REM sleep (right). Processed LFP signals for P-wave detection (red) are also shown.

Figure 2. A P-wave detection method and the evaluation.

(**A**) An automated P-wave detection algorithm.

(**B**) Example traces of pontine EEGs.

(**C**) Average waveforms of P-waves. blue, P-waves during NREM sleep; green, P-waves during REM sleep.

(**D**) Detected individual P-waves represented in first two principal component space.

(**E**) Comparisons of average waveforms of P-waves between sleep states based on Pearson's correlation coefficient ($n = 16$, $r = 0.97 \pm 0.01$).

(**F**) Comparisons of the number of detected P-waves across different electrode distances. The effect of electrode distances was significant ($H(7) = 257.4$, $p < 0.05$, Kruskal-Wallis test).

Figure 3. Features of P-waves in mice.

(**A**) Comparison of P-wave frequency between sleep states. $n = 35$ recordings. *** $p < 0.0001$, rank sum test.

(**B**) Comparison of inter-event intervals between sleep states. inset, comparison of the medial intervals of P-waves between states. $n = 35$ recordings, *** $p < 0.0001$, rank sum test.

(**C**) Cross-correlations of bilateral P-waves. $n = 9$ recordings.

(**D**) Temporal evolution of P-wave frequency around REM sleep onset (left) and offset (right). $n = 99$ REM sleep episodes.

(**E**) The relationship between P-wave frequency and sleep episode duration. Lines are linear regression lines. Bottom, distributions of P-wave frequency during NREM (blue) and REM sleep (green).

Figure 4. Brainstem neural firing during P-waves.

(**A**) Normalized average firing profiles across cells during NREM (left) and REM sleep (right). Cells were sorted by the peak timing during REM sleep. Color bar indicates cell numbers in panel (C).

(**B**) Comparisons of mean firing profiles between sleep states across cells based on Pearson's correlation coefficient. *** $p < 0.0001$, t-test.

(**C**) Mean firing profiles of individual neurons during REM sleep represented in first two PC space. Color indicates the order of the peak timing during REM sleep (A).

(**D**) First three PCs and explained variability.

Figure 5. Functional coupling between P-waves and SWRs during NREM sleep.

(**A**) A diagram of the experimental approach for hippocampal population recording with pontine EEG monitoring, showing a cortical EEG electrode, a bipolar electrode for pontine EEG, a 32-channel silicon probe for hippocampal population recording.

(**B**) Temporal profiles of SWRs (blue) and P-waves across NREM and REM sleep episodes. Each episode duration was divided into four discrete time bins as normalized time windows.

(**C**) Cross-correlation between SWRs and P-waves during NREM sleep. n = 4 recordings.

(**D**) Cross-correlation between ripple (140-250 Hz) power profile and P-waves during NREM sleep. Each cross-correlation profile was z-scored based on the profile in -3~-2 sec window.

(**E**) Comparison of SWR duration between SWRs coupled with P-waves within 30 ms and other SWRs. *** $p < 0.0005$, rank sum test.

(**F**) Mean activity profiles of CA1 neurons relative to P-wave timing during NREM sleep. Cells were sorted by their first PC score.

Figure 6. Functional coupling between P-waves and hippocampal activity during REM sleep.

(**A**) The average hippocampal LFPs triggered by P-wave timing.

(**B**) A scalogram of P-wave-triggered hippocampal LFPs.

(**C**) A phase diagram of P-wave timing relative to hippocampal theta rhythms.

(**D**) Normalized average firing profiles across CA1 neurons relative to P-wave timing during REM sleep. Cells were sorted by the peak timing. Color bar indicates cell numbers in panel (E).

(**E**) Mean firing profiles of individual CA1 neurons relative to P-wave timing represented in first two PC space. Color indicates the order of the peak timing (D).

(**F**) First three PCs and explained variability.